

# ADVANCED MATERIALS

## Supporting Information

for *Adv. Mater.*, DOI: 10.1002/adma.202209333

Non-Destructive Low-Temperature Contacts to MoS<sub>2</sub>  
Nanoribbon and Nanotube Quantum Dots

*Robin T. K. Schock, Jonathan Neuwald, Wolfgang  
Möckel, Matthias Kronseder, Luka Pirker, Maja  
Remškar, and Andreas K. Hüttel\**

# Non-destructive low-temperature contacts to MoS<sub>2</sub> nanoribbon and nanotube quantum dots

## Supporting Information

R. T. K. Schock,<sup>1</sup> J. Neuwald,<sup>1</sup> W. Möckel,<sup>1</sup> M. Kronseder,<sup>1</sup> L. Pirker,<sup>2,3</sup> M. Remškar,<sup>2</sup> and A. K. Hüttel<sup>1, a)</sup>

<sup>1)</sup>*Institute for Experimental and Applied Physics, University of Regensburg, 93040 Regensburg, Germany*

<sup>2)</sup>*Solid State Physics Department, Jožef Stefan Institute, 1000 Ljubljana, Slovenia*

<sup>3)</sup>*J. Heyrovský Institute of Physical Chemistry, v.v.i., Czech Academy of Sciences, 182 23 Prague, Czech Republic*

(Dated: 15 December 2022)

### CONTENTS

<b>I. Fabrication</b>	1
<b>II. Additional information on the measured devices</b>	2
<b>III. Differentiating nanoribbons and nanotubes</b>	3
<b>IV. Mechanism of semimetal based contacts to transition metal dichalcogenides</b>	3
<b>V. Influence of bismuth thickness on the two terminal resistance</b>	3
<b>VI. Low temperature I(V) characteristics</b>	4
<b>VII. Larger plots of Fig. 5(e) of the main text</b>	6
<b>References</b>	6

### I. FABRICATION

At the starting point of our fabrication, the MoS<sub>2</sub> nanomaterial is grown via a slow chemical transport reaction using iodine as a transport agent.<sup>1,2</sup> Source material and transport agent is placed at one end of a glass ampoule; the ampoule is evacuated, molten closed, and placed into a tube oven. There, a temperature gradient is maintained for several weeks to drive the chemical transport reaction. It produces MoS<sub>2</sub> flakes as well as nanoribbons and nanotubes of a wide range of diameter, as shown in Fig. 1 of the main text and Fig. S-1.

Using a wafer dicing tape with low adhesion (Nitto Denko ELP BT-150E-CM), as also common in the preparation of 2D materials, the nanomaterial is transferred onto a silicon substrate.<sup>3</sup> We use a highly p+ (boron) doped silicon wafer which remains conductive at low temperature and can thus act as a back gate. Its surface is covered with a 500 nm thick thermally grown oxide and a standard pattern of pre-defined grid markers also used by other researchers in Regensburg,<sup>4</sup> see Fig. 1(c) of the main text and Figs. S-1(a,e). The distance between the cross-shaped position markers is 50 μm.

The transfer result is imaged in an optical microscope, see Fig. S-1(a,e), and typically shows on the silicon oxide surface both flakes of varying size and thickness and quasi-one dimensional structures. Interestingly, MoS<sub>2</sub> nanotubes and nanoribbons are clearly visible in optical images using a 100x objective for widths down to 30 nm. While scanning electron microscopy might provide more precise images, it can lead to contamination and trapped charges and is thus avoided at this stage of the fabrication process.

After selection of suitable quasi-one dimensional structures and design of electrode geometries, a single layer of polymethyl methacrylate (PMMA) of molecular weight 200k, 9% solved in anisole is then spin-coated onto the chip and subsequently baked

---

<sup>a)</sup>Electronic mail: andreas.huettel@ur.de

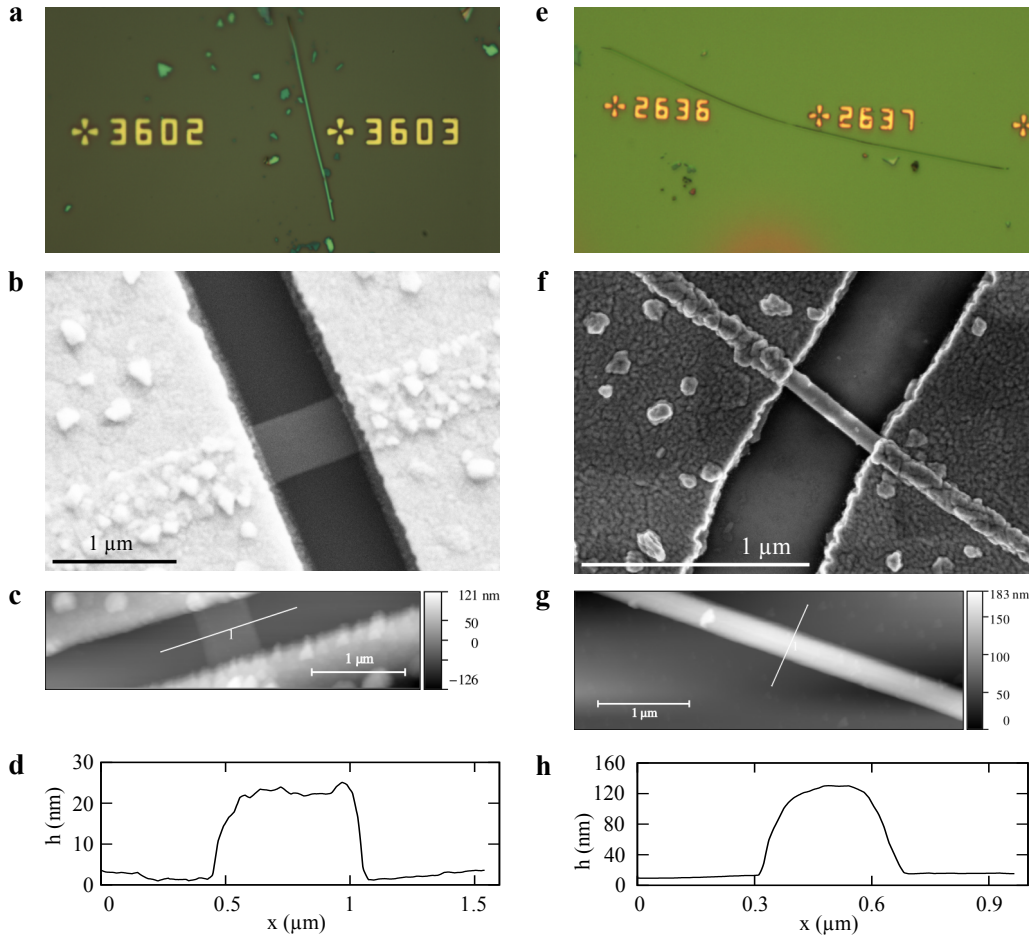


FIG. S-1. Comparison of a nanoribbon and a nanotube device. (a-d) device A (nanoribbon), (e-h) device B (nanotube). (a,e) optical microscope image after transfer; (b,f) SEM image of the finished device; (c,g) AFM image of the active device region; (d,h) AFM trace cut across the MoS<sub>2</sub> nanostructure. Note the different axis scaling.

out on a hot plate for 5 minutes at 150°C. Standard electron beam lithography is then used to define the contacts, followed by development for 90s in a 1:3 mixture of methyl isobutyl ketone (MIBK) and isopropyl alcohol (IPA).

As contact material we use a 25 nm  $\lesssim d \lesssim$  45 nm bismuth layer capped with 100 nm gold,<sup>5</sup> see Table S-1 for the device-specific values.

For most measured devices, and in particular devices B–H, the materials are deposited using electron-beam assisted evaporation at  $p \sim 10^{-7}$  mbar, with typical deposition rates of 0.5 Å/s for bismuth and 1 Å/s for gold, respectively. No cooling or heating of the sample holder was performed.

The contact materials of device A were deposited in a molecular beam epitaxy chamber. The substrate was neither cooled nor strongly heated. 30 nm bismuth was grown at 50°C manipulator temperature, 400°C bismuth source cell temperature, and a chamber pressure of  $p < 10^{-10}$  mbar while rotating the sample. Subsequently 10 nm gold was grown at 70°C manipulator temperature, 1270°C gold source cell temperature, and a chamber pressure of  $p \sim 5 \cdot 10^{-10}$  mbar, while rotating the sample. This was followed up by the deposition of an additional 80 nm gold in a UHV evaporator.

In either case lift-off is subsequently carried out in hot acetone.

## II. ADDITIONAL INFORMATION ON THE MEASURED DEVICES

Table S-1 lists additional information on the structural and electrostatic parameters of the characterized devices.

Device	$L$ (nm)	$w$ (nm)	$h$ (nm)	$d_{\text{Bi}}$ (nm)	$R_{\text{RT}}$ (k $\Omega$ )	$E_C$ (meV)	$\alpha$	$C_g$ (aF)	$C_{\text{th}}^{\text{pl}}$ (aF)	$C_{\text{th}}^{\text{cyl}}$ (aF)	$V_g^{\text{min}}$ (V)	$V_g^{\text{max}}$ (V)	$\sim V_g^{\text{gap}}$ (V)	$\Delta V_{\text{SD}}^0$ (mV)	gap	R/T
A	270 $\pm$ 20	500 $\pm$ 300	18 $\pm$ 2	30	97	0.25	0.0031	2.0	9.3	0.8	-65	30	-19	0.01	yes	R
B	150 $\pm$ 20	90 $\pm$ 20	115 $\pm$ 7	38	43	1.1	0.0047	0.72	0.93	0.41	-80	24	—	0.005	no	T
C	200 $\pm$ 20	155 $\pm$ 30	20 $\pm$ 10	45	250	1.85	0.0052	0.46	2.1	0.56	-10	10	—	0.05	no?	R
D	220 $\pm$ 30	360 $\pm$ 40	20 $\pm$ 10	25	178	2.1	0.021	1.6	12.6	0.9	0	22	-4	0.2	yes	R
E	950 $\pm$ 350	380 $\pm$ 40	15 $\pm$ 2	25	180	—	—	—	—	—	-30	40	2	2.5	yes	R
F	220 $\pm$ 20	90 $\pm$ 20	115 $\pm$ 7	38	153	—	—	—	—	—	0	30	—	7.5	no?	T
G	1300 $\pm$ 50	81 $\pm$ 20	74 $\pm$ 5	38	900	—	—	—	—	—	—	—	—	—	—	T
H	360 $\pm$ 50	142 $\pm$ 25	14 $\pm$ 4	38	480	—	—	—	—	—	—	—	—	—	yes	R

TABLE S-1. Extended table of the structural and electrostatic parameters of the characterized devices: segment/channel length  $L$ , width  $w$ , height  $h$  from AFM measurement, bismuth layer thickness  $d_{\text{Bi}}$ , room temperature resistance  $R_{\text{RT}}$  at  $V_g = 0$ , typical low-temperature charging energy  $E_C$ , gate conversion factor  $\alpha = C_g/C_\Sigma$  where  $C_\Sigma$  is the total capacitance of the quantum dot, gate capacitance  $C_g$  extracted from Coulomb blockade, model gate capacitance values  $C_{\text{th}}^{\text{pl}}$  (plate capacitor model) and  $C_{\text{th}}^{\text{cyl}}$  (wire over plane model), minimal and maximal tested gate voltage, band gap onset gate voltage  $V_g^{\text{gap}}$ , size of the low bias region without conductance at low temperature  $\Delta V_{\text{SD}}^0$ , presence of a band gap, and characterization of the device as nanoribbon (R) or nanotube (T). Devices C and F did not display a band gap, were however not tested far into negative gate voltages. Device G is the bismuth-based device of Fig. 2(b) of the main text, device H the device measured in Fig. 2(c) of the main text (both room temperature characterization only).

### III. DIFFERENTIATING NANORIBBONS AND NANOTUBES

Figure S-1 displays for comparison a nanoribbon device (device A) and a nanotube device (device B), cf. also Fathipour et al.<sup>6</sup> In each case, an optical microscope image, an SEM image, and an AFM image with trace cut is provided. Note the different axis scaling; while the ribbon has a height of 18 nm and a width of approximately 500 nm, the nanotube is much more prominent with a height of 115 nm compared to an apparent width of similar scale.

### IV. MECHANISM OF SEMIMETAL BASED CONTACTS TO TRANSITION METAL DICHALCOGENIDES

Electronic devices based on transition metal dichalcogenide (TMDC) nanomaterials have so far been severely limited by contact resistances. The primary origin of these contact resistances is the formation of Schottky barriers<sup>7</sup> at the metal-semiconductor interface, due to a) a mismatch of the material work function<sup>8</sup> and b) metal-induced gap states (MIGS) leading to Fermi level pinning.<sup>9,10</sup>

In a MoS<sub>2</sub>–metal contact, the Fermi level is typically pinned to a position close to the conduction band edge.<sup>11,12</sup> The straightforward approach to achieve an Ohmic contact is to pick a contact metal with a low electronic work function. Typically, best results have been observed using titanium or scandium.<sup>3,8</sup> This however leads to a different problem: metals with low work function are highly reactive; titanium, e.g., has a higher affinity to the surface sulphur atoms of MoS<sub>2</sub> than molybdenum. As atomically resolved spectroscopy has shown,<sup>13</sup> surface deposition of titanium alone is sufficient to destroy the MoS<sub>2</sub> crystal lattice several layers deep. Particularly in low temperature applications, random potentials and charge traps below the contacts are the inevitable consequence.<sup>3</sup>

Recently, Shen *et al.*<sup>5</sup> have found a solution to this problem. Fermi level pinning is here caused by so-called metal-induced gap states in the semiconductor,<sup>9,12</sup> see also Fig. S-2, resulting from the hybridization with electronic states in the metal at the Fermi energy. Replacing the metal with a semimetal, where the density of states reduces to zero at the Fermi energy, avoids or at least strongly suppresses this hybridization and thereby the metal-induced gap states.<sup>5</sup> At room temperature, Shen *et al.* were able to demonstrate highly Ohmic contacts to planar MoS<sub>2</sub> using a bismuth-gold bilayer.

### V. INFLUENCE OF BISMUTH THICKNESS ON THE TWO TERMINAL RESISTANCE

Figure S-3 shows the two-terminal resistance of multiple nanotube and nanoribbon segments, plotted as function of the thickness of the deposited bismuth layer. As in Fig. 2(a) of the main text, the measured values scatter widely. The resistance is expected to display a minimum for a certain thickness  $d_{\text{Bi}}$ : at lower values the MoS<sub>2</sub> is not fully covered, leading to Fermi level pinning effects and the formation of Schottky barriers, while at higher values the semimetal itself hinders transport via a series resistance.

Testing initially started with thin layers and the thickness was increased stepwise. As expected from above arguments, the resistances initially slightly decreased. Once an increase was observed again, this fabrication series was stopped. A systematic test of the impact of the layer thickness would require more data points for thicker layers.

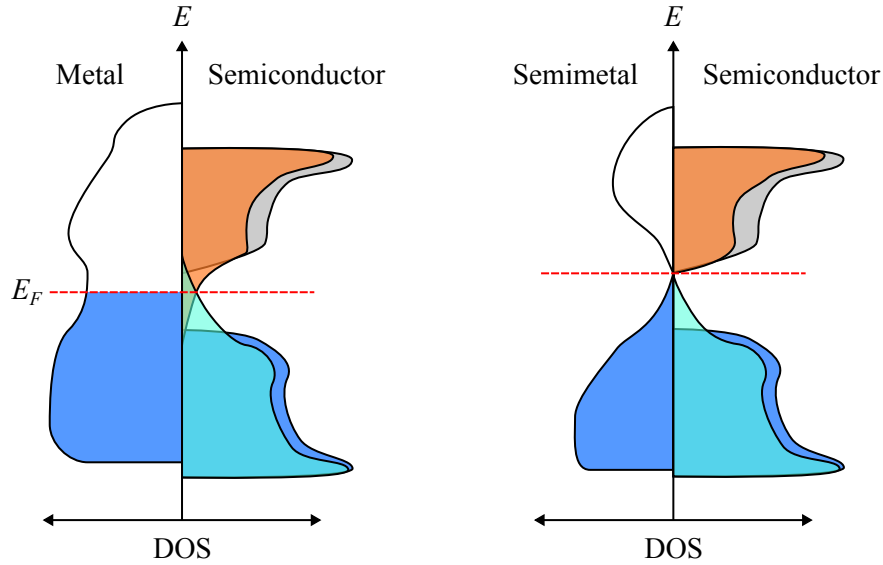


FIG. S-2. Metal-induced gap states at the Fermi energy  $E_F$  in a metal-semiconductor interface, and their suppression in a semimetal-semiconductor interface.<sup>5</sup>

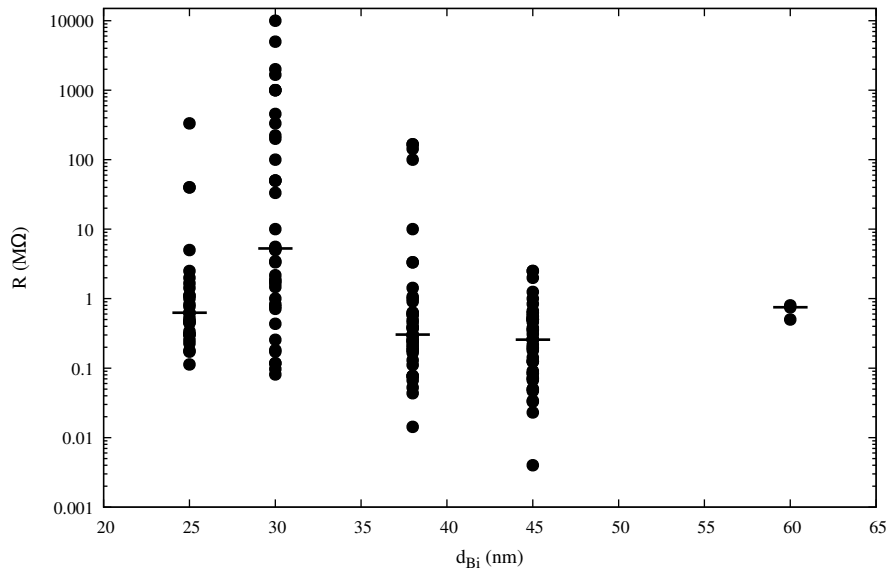


FIG. S-3. Two-terminal room temperature resistance of multiple nanotube and nanoribbon segments, plotted against the thickness of the deposited bismuth layer. The lowest median resistances (horizontal lines) and lowest resistances overall are found at  $d_{\text{Bi}} = 38$  nm and 45 nm.

## VI. LOW TEMPERATURE I(V) CHARACTERISTICS

At cryogenic temperatures, Coulomb blockade dominates the electronic nonlinearity at energy scales comparable to the charging energy. This is illustrated in Fig. S-4, plotting  $I(V_{\text{SD}})$  traces from the measurement of Fig. 3(a) in the main text at fixed gate voltages  $V_g = -21, -20, -19, -18.035$  V. For  $V_g = -21, -20, -19$  V the equidistant traces cut at random position through the Coulomb blockade regions, resulting in characteristic zero current for sufficiently low bias. The trace at  $V_g = -18.035$  V is chosen such that at this gate voltage the tips of the single electron tunneling region in the inset of Fig. 3(a) reach the zero-bias line. Here, the region of low-bias Coulomb blockade is fully absent (see also the inset of Fig. S-4 with a detail enlargement). Steps in the low-bias current hint at possible discrete levels, see also Fig. 5(e) in the main text and its discussion.

Figure S-5 shows a measurement of device A at positive gate voltage, with a logarithmic color plot of the absolute value

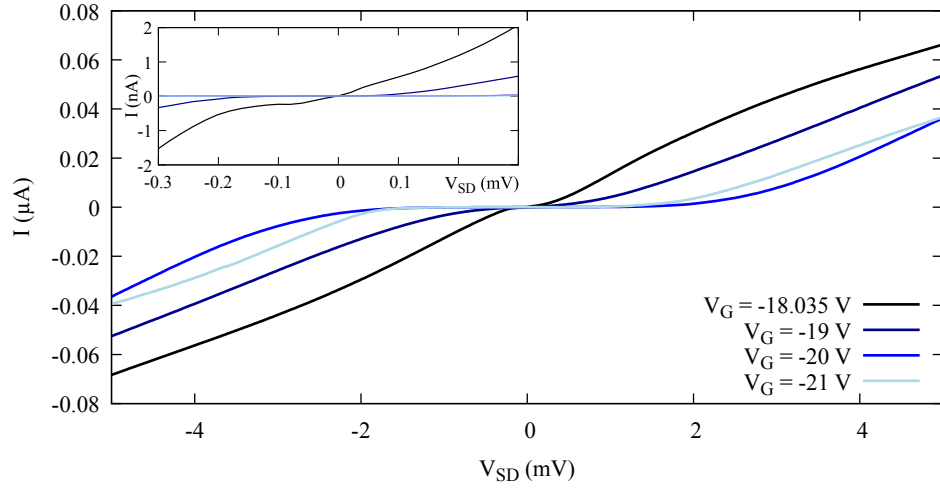


FIG. S-4. Source-drain current traces  $I(V_{SD})$  at fixed gate voltage  $V_g$  of device A, from the measurement plotted in Fig. 3(a) of the main text. Inset: detail zoom around  $V_{SD} = 0$ .

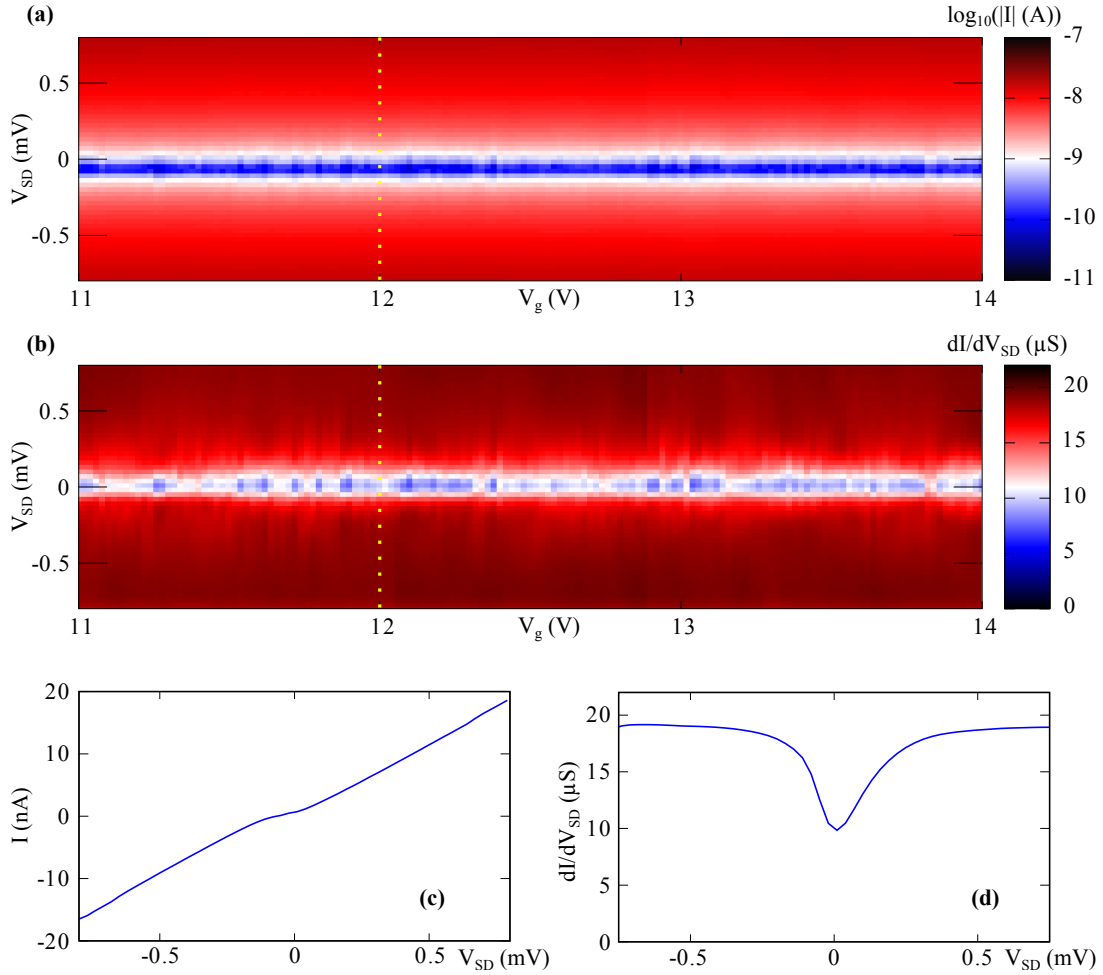


FIG. S-5. Example low-temperature measurement of device A at large positive gate voltage. (a) Absolute value of the current  $|I(V_g, V_{SD})|$  in logarithmic color scale. (b) Differential conductance  $dI/dV_{SD}(V_g, V_{SD})$  in linear color scale. (c), (d) Trace cuts from (a) and (b) at  $V_g = 12$  V.

of the current  $|I(V_g, V_{SD})|$  as function of gate voltage  $V_g$  and bias voltage  $V_{SD}$  in Fig. S-5(a) and a linear plot of the differential conductance  $dI/dV_{SD}(V_g, V_{SD})$  in Fig. S-5(b). Trace cuts of both plots at fixed gate voltage  $V_g = 12$  V are shown in Figs. S-5(c,d).

While a region of lower conductance is still visible for  $|V_{SD}| < 0.1$  mV, the conductance minimum is in the range of  $5 \mu\text{S} \leq G \leq 10 \mu\text{S}$ , above typical values for Coulomb blockade. The low-bias pattern resembles observations of Fabry-Pérot interference in carbon nanotubes.<sup>14,15</sup> At  $|V_{SD}| \geq 0.1$  mV, the differential conductance is approximately constant, i.e., the current increases linearly with bias voltage  $V_{SD}$ .

## VII. LARGER PLOTS OF FIG. 5(E) OF THE MAIN TEXT

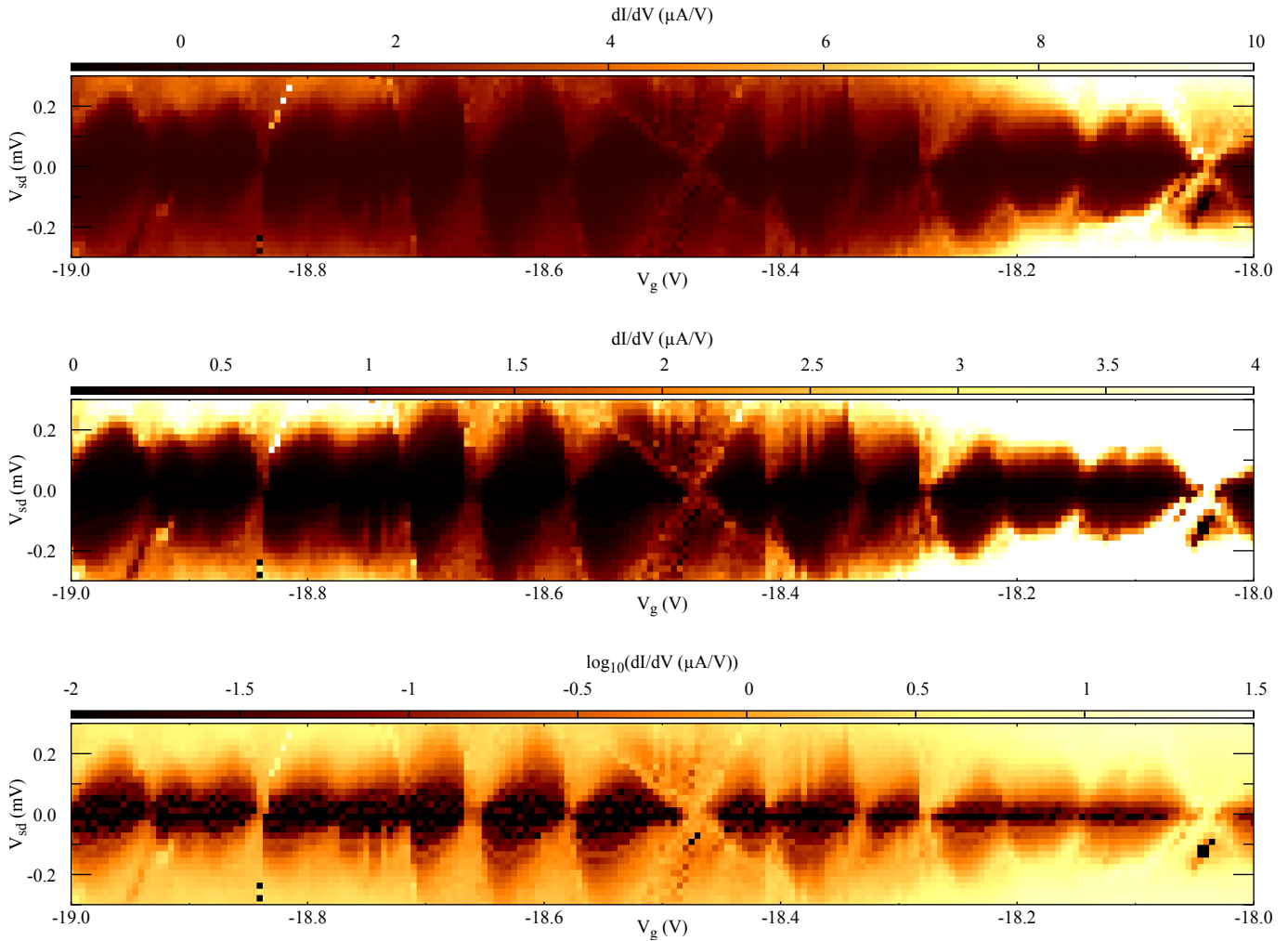


FIG. S-6. Larger plots of the data of Fig. 5(e) of the main text, in different linear and in logarithmic color scale.

## REFERENCES

- <sup>1</sup>M. Remskar, Z. Skraba, F. Cléton, R. Sanjinés, and F. Lévy, “MoS<sub>2</sub> as microtubes,” *Applied Physics Letters* **69**, 351–353 (1996).
- <sup>2</sup>M. Remskar, “Inorganic nanotubes,” *Advanced Materials* **16**, 1497–1504 (2004).
- <sup>3</sup>S. Reinhardt, L. Pirker, C. Bäuml, M. Remskar, and A. K. Hüttel, “Coulomb blockade spectroscopy of a MoS<sub>2</sub> nanotube,” *physica status solidi (RRL) – Rapid Research Letters* **13**, 1900251 (2019).
- <sup>4</sup>R. Huber, M.-H. Liu, S.-C. Chen, M. Drienovsky, A. Sandner, K. Watanabe, T. Taniguchi, K. Richter, D. Weiss, and J. Eroms, “Gate-tunable two-dimensional superlattices in graphene,” *Nano Letters* **20**, 8046–8052 (2020).

- <sup>5</sup>P.-C. Shen, C. Su, Y. Lin, A.-S. Chou, C.-C. Cheng, J.-H. Park, M.-H. Chiu, A.-Y. Lu, H.-L. Tang, M. M. Tavakoli, G. Pitner, X. Ji, Z. Cai, N. Mao, J. Wang, V. Tung, J. Li, J. Bokor, A. Zettl, C.-I. Wu, T. Palacios, L.-J. Li, and J. Kong, "Ultralow contact resistance between semimetal and monolayer semiconductors," *Nature* **593**, 211–217 (2021).
- <sup>6</sup>S. Fathipour, M. Remskar, A. Varlec, A. Ajoy, R. Yan, S. Vishwanath, S. Rouvimov, W. S. Hwang, H. G. Xing, D. Jena, and A. Seabaugh, "Synthesized multiwall MoS<sub>2</sub> nanotube and nanoribbon field-effect transistors," *Applied Physics Letters* **106**, 022114 (2015).
- <sup>7</sup>W. Schottky, "Zur Halbleitertheorie der Sperrschicht- und Spitzengleichrichter," *Zeitschrift für Physik* **113**, 367–414 (1939).
- <sup>8</sup>S. Das, H.-Y. Chen, A. V. Penumatcha, and J. Appenzeller, "High performance multilayer MoS<sub>2</sub> transistors with scandium contacts," *Nano Letters* **13**, 100–105 (2013).
- <sup>9</sup>S. G. Louie and M. L. Cohen, "Electronic structure of a metal-semiconductor interface," *Physical Review B* **13**, 2461–2469 (1976).
- <sup>10</sup>Y. Guo, D. Liu, and J. Robertson, "3D Behavior of Schottky Barriers of 2D Transition-Metal Dichalcogenides," *ACS Applied Materials & Interfaces* **7**, 25709–25715 (2015).
- <sup>11</sup>C. Gong, L. Colombo, R. M. Wallace, and K. Cho, "The unusual mechanism of partial Fermi level pinning at metal–MoS<sub>2</sub> interfaces," *Nano Letters* **14**, 1714–1720 (2014).
- <sup>12</sup>K. Sothewes, R. van Bremen, E. Dollekamp, T. Boulogne, K. Nowakowski, D. Kas, H. J. W. Zandvliet, and P. Bampoulis, "Universal Fermi-level pinning in transition-metal dichalcogenides," *The Journal of Physical Chemistry C* **123**, 5411–5420 (2019).
- <sup>13</sup>R. J. Wu, S. Udyavara, R. Ma, Y. Wang, M. Chhowalla, T. Birol, S. J. Koester, M. Neurock, and K. A. Mkhoyan, "Visualizing the metal-MoS<sub>2</sub> contacts in two-dimensional field-effect transistors with atomic resolution," *Physical Review Materials* **3**, 111001 (2019).
- <sup>14</sup>W. Liang, M. Bockrath, D. Bozovic, J. H. Hafner, M. Tinkham, and H. Park, "Fabry-Pérot interference in a nanotube electron waveguide," *Nature* **411**, 665–669 (2001).
- <sup>15</sup>A. Dirnacher, M. del Valle, K. Götz, F. Schupp, N. Paradiso, M. Grifoni, C. Strunk, and A. K. Hüttel, "Secondary electron interference from trigonal warping in clean carbon nanotubes," *Physical Review Letters* **117**, 166804 (2016).